Amplitude and horizontal structure of a large diurnal sea surface warming event during the Coastal Ocean Dynamics Experiment

P. Flament, J. Firing, M. Sawyer and C. Trefois
Department of Oceanography
University of Hawaii at Manoa

Abstract. Intense diurnal warming of the ocean surface was observed in April 1982 off California, using a combination of mooring, hydrographic and satellite infrared and satellite pigment measurements. The event corresponded to a spatial and temporal minimum of the wind stress. The diurnal surface temperature amplitude exceeded 6.6 C locally despite a 490-nm optical depth of $\sim$20 m, suggesting that phytoplankton was not responsible for the shallow heat trapping. Coherent horizontal temperature streaks at least 50 km long and 4 to 8-km wide formed during the subsequent erosion of the shallow warm layers. It is hypothesized that their scale was set by planetary boundary layer circulations.

Contents

1 Introduction

Intense diurnal warming of the surface of the ocean commonly occurs in low wind conditions, when the wind-driven turbulence is insufficient to erode the near-surface restratification caused by absorption of solar radiation. A layer of warm water is then observed to cap the homogeneous mixed-layer left by previous mixing events, with a typical thickness of 2 to 5 m and a temperature anomaly of 1 to 4 C (e.g. Bruce and Firing [1974]). In contrast, when an active wind-driven mixed layer is present, the diurnal amplitude of surface temperature seldom exceeds a few tenths of degrees. Regions where the diurnal amplitude of surface temperature reaches these extreme values extend over vast areas corresponding closely to anticyclonic ridges in the atmosphere (e.g. Cornillion and Strama [1985]).

In this paper, we present a case study of diurnal warming off Northern California, using 1-km resolution satellite images and *in-situ* data collected during the Coastal Ocean Dynamics Experiment (CODE) [Lentz, 1987]. We will show that (1) the warming event corresponded closely to a spatial and temporal wind-stress minimum, (2) the diurnal amplitude of surface temperature exceeded 6.5 C locally despite a 490-nm optical depth of 15 to 25 m, and (3) coherent horizontal temperature streaks formed at scales of 4 to 8 km during the subsequent erosion of the warming layers. The *in-situ* and satellite measurements are presented in sections 2 and 3 respectively. The observations are summarized in section 4 and discussed in section 5. Details concerning the processing of satellite data are discussed in the Appendix.

2 Mooring and hydrographic measurements.

In April 1982, a large anticyclone centered at 145° W 43° N covered the Northeast Pacific, driving upwelling-favorable winds along the coast of California. The so-called spring transition to the summer ocean circulation regime at the CODE site began on 15 April [Lentz, 1987], with the onset of a strong equatorward wind which persisted for 5 days. On 20 April at 08:00 UT, a ridge extended southwestward from the anticyclone (Fig. 1), resulting in a relaxation of the pressure gradient until 23 April at 00:00 UT, when the equatorward wind progressively resumed.

The positions of six CODE moorings and two NDBO moorings that provided meteorological measurements are shown in Fig. 2 (*cf.* Limeburner, [1985]). Fig. 3 shows time series of net surface heat flux, wind stress, air temperature, and water temperature at 0, 10 and 20 m depth, from 18 April to 29 April at mooring C-5 (123° 40.3W 38° 30.8N). Note that Local Solar Time (LST) lags Universal Time (UT) by $\sim$8 hours. Mooring C-5 is chosen because it is the furthest from the coast; closer to the coast, the diurnal cycle is increasingly affected by coastal processes such as sea- and land breezes (*cf.* Beardsley *et al.* [1987], their Figs. 5-6). To study the essentially one-dimensional diurnal warming process, we try to avoid the coastal influences as much as possible.

The net heat flux was dominated by radiation heating during the daylight period (0.55 day), peaking at $\tilde{7}80$ $\mathrm{W}m^{-2}$, and by radiative/evaporative cooling at night, varying between -125 and -70 $\mathrm{W}m^{-2}$, with an average net daily heat input of 18 $\mathrm{W}m^{-2}$. The computations of the heat fluxes were discussed by Lentz [1987]; the incident short wave radiation flux was computed from direct measurements, the sensible heat flux was computed using the bulk formula, whereas the net long-wave radiation flux and the latent heat flux were parameterized based on the surface water temperature (the short wave radiometer on C-5 failed early; the net fluxes from nearby moorings

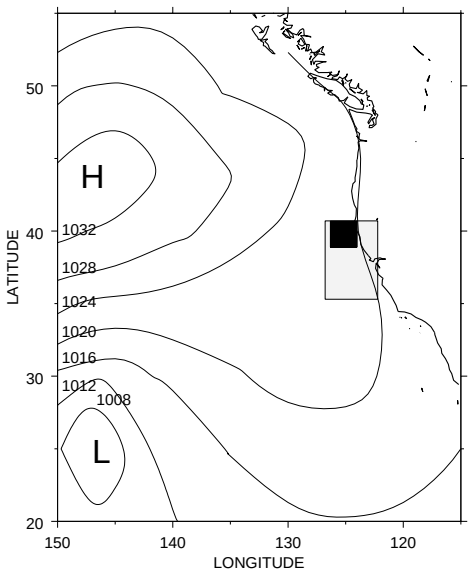

Figure 1: Map of the surface pressure field on 20 April 1982 at 16:00 UT. Note the anticyclonic ridge extending southeastward from 145°W 43°N. The position of the images shown in Fig. 8 is shaded; the position of the enlarged images shown in Fig. 12 is solid black.

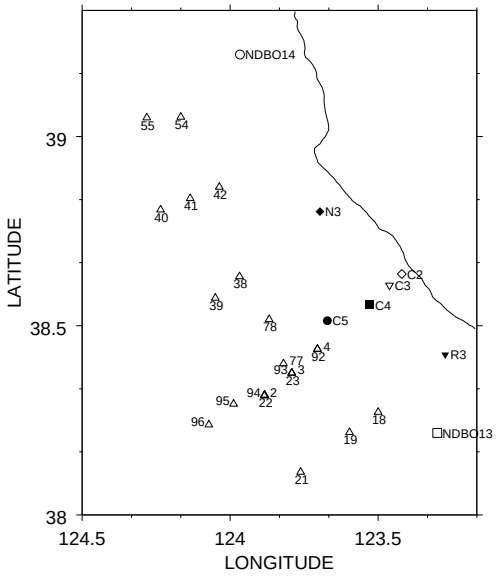

Figure 2: Map showing the positions of the CODE and NDBO moorings, and of the *R/V Wecoma* CTD stations (Δ) that were more than 35 km from the coast.

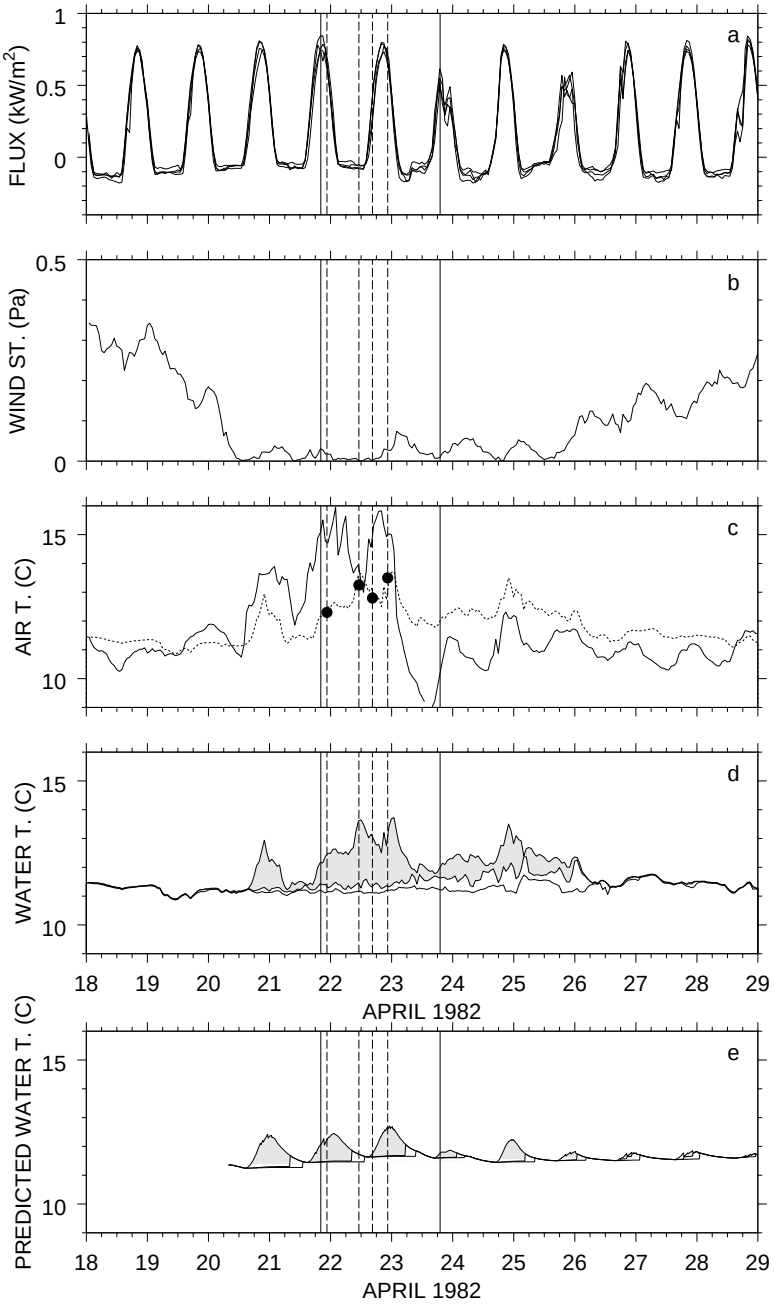

Figure 3: Moored time series during the wind relaxation event. All series are from mooring C-5 except the top panel. (a) net surface heat fluxes at moorings N-3, C-2, C-3 and R-3; (b) wind stress; (c) air temperature (solid) and surface water temperature (dashed), with the satellite temperatures shown by ; (d) observed water temperature at the surface, 10 and 20 m depths (shaded between the surface and 10 m); (e) predicted water temperature at 0.5 (surface), 10 and 20 m depths. The times of the AVHRR and CZCS satellite images are shown by dashed and solid lines respectively.

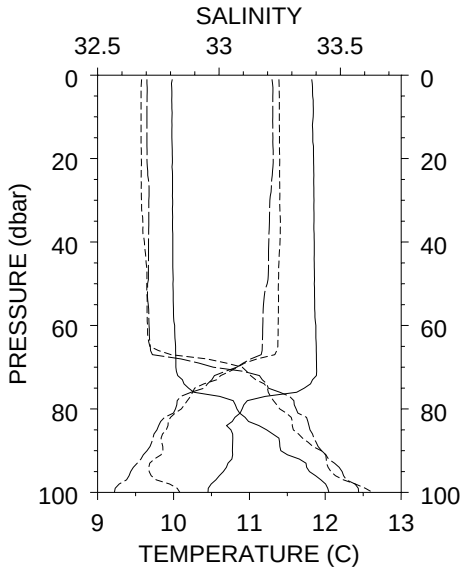

Figure 4: Profiles of temperature and salinity at CTD stations 2 (solid), 3 (short dashed) and 4 (long dashed), in the vicinity of C-5, prior to the wind relaxation. See Fig. 2 for the positions of the stations.

N-3, C-2, C-3 and R-3 are well correlated, and are presumably a good approximation to the net flux at C-5).

The wind stress (estimated using a constant drag coefficient of 1.2×10^{-3}) dropped from more than 0.2 Pa to less than 0.005 Pa at the start of the calm period, and remained less than 0.03 Pa at the times of the satellite images. During the periods of strong wind before 20 April and after 27 April, a surface mixed-layer was present, as shown by the time series of water temperatures at different depths collapsing into a single trace (the offset corrections of Lentz and Trowbridge, 1991, were applied to the mooring temperatures). Diurnal warming shallower than 10 m and reaching 2.2 C at C-5 occurred between 20 April and 24 April.

During this calm period, the *R/V Wecoma* conducted a CTD hydrographic survey [Fleischbein *et al.*, 1983]; the positions of the hydrographic stations at least 35 km from the coast are shown in Fig. 2. A mixed layer deeper than 65 m was observed at stations 2, 3 and 4 on 20 April, before the wind relaxation (Fig. 4). Fig. 5 shows profiles of salinity anomaly and temperature anomaly referenced to 25 m depth, for stations between 20 April and 24 April. Salinity is constant before as well as during the wind relaxation event. Warm surface layers, initially less than 5 m deep with temperature anomalies reaching 2 C, appeared on April 21, and had propagated to nearly 15 m depth by April 24 (the actual surface temperature anomalies may be larger because the CTD profiles started at only 1-2 m depth, with no higher resolution sampling of the upper meter).

Fig. 6 is a time series of anomalous heat content, integrated between the surface and 25 m depth, for the CTD stations shown in Fig. 5. The integrated net heat fluxes from the mooring time series (*cf.* Fig. 3) are also shown. The anomalous heat content at the end of the calm period is surprisingly well accounted for by the integrated net heat flux, although there is scatter among the stations, most

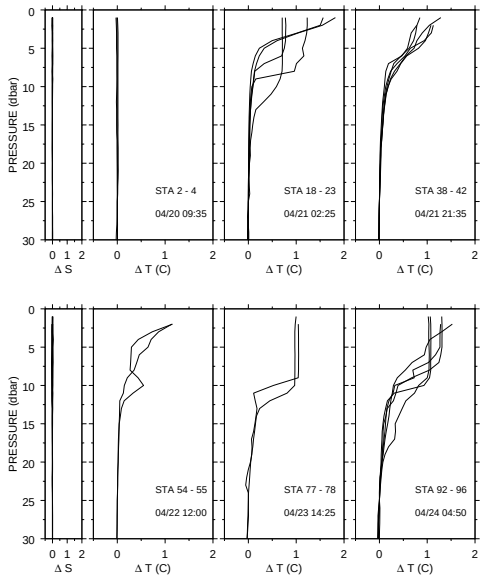

Figure 5: Salinity and temperature anomalies, referenced to 25 m depth, for the CTD stations shown in Fig. 2. The stations are grouped in six temporal clusters. The mean UT of each cluster is given.

likely due to mesoscale variability within the fairly large domain sampled by the CTD survey.

Fig. 7 is a scatter plot of net daily heat input versus diurnal amplitude of surface temperature for the CODE moorings. The amplitude ranges between 1 C and 3 C at most moorings, but reaches 3.5 C at C-2 and 5.-5 C at NDBO-14 (these values may be underestimated, because the "surface" thermistor is generally placed at 0.3 to 0.6 m below the surface, and may be affected by mixing in the wake of the buoy). For reference, the heat contents between the surface and 25 m depth for the CTD stations are also shown. Stations early in the relaxation period (i.e. 18 and 19) fall close to the mooring points, but at later stations, the heat content accumulated since the start of the calm period is, of course, larger than the daily heat input.

To further quantify this warming event, we ran a bulk mixed layer model following Price *et al.* [1986], forced with the heat fluxes from mooring C-3, the wind stress measured at C-5, and initialized with a 65-m deep mixed layer on 20 April (*cf.* Fig. 4). This model has been extensively tested under similar highly stratified conditions. The downward irradiance was parameterized as a double exponential $I(z)/I_0 = Re^{\zeta_1 z} + (1-R)e^{\zeta_2 z}$ where I_0 is the surface insolation, $\zeta_1^{-1} = 1.5\mathrm{m}$ and $\zeta_2^{-1} = 14\mathrm{m}$ are attenuation lengths for a Jerlov type II water, and $R = 0.77$ (Paulson and Simpson, 1977). The vertical resolution was set at 10 cm and the time step at 0.001 day. The time series of predicted water temperatures are shown in Fig. 3e ($3 \times 10^{0.5}$ m depth was chosen as representative of the "surface temperature", given the ~ 0.6 m sampling depth of the surface thermistor). The model reproduces the diurnal variations of stratification reasonably well. Divergence from the measurements is most noticeable on 22 April around 11:00 UT, when a large night time temperature peak is observed, obviously due to lateral advection rather than to local heating; departures from a one-dimensional balance were also reported by Price *et al.* [1986, their Fig. 1].

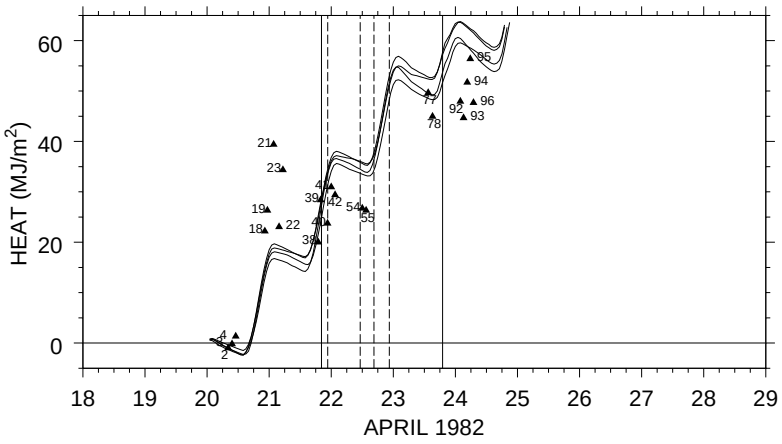

Figure 6: Integrated temperature anomalies referenced to 25 m depth for the CTD stations, expressed as a heat content, and time series of integrated net surface heat flux from the moorings. The times of the satellite images are shown (*cf.* Fig. 3).

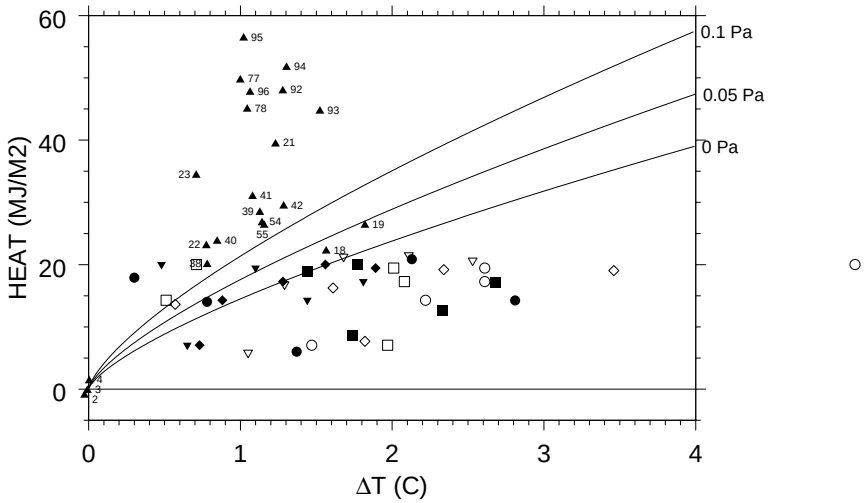

Figure 7: Scatter plot of daily heat input versus diurnal amplitude of surface temperature for the CODE moorings, represented by the same symbols as in Fig. 2. The empirical relationship between heat input and temperature anomaly given by Price *et al.* [1987] is shown for wind stresses of 0, 0.05 and 0.1 Pa. The anomalous heat content for the CTD stations is also shown.

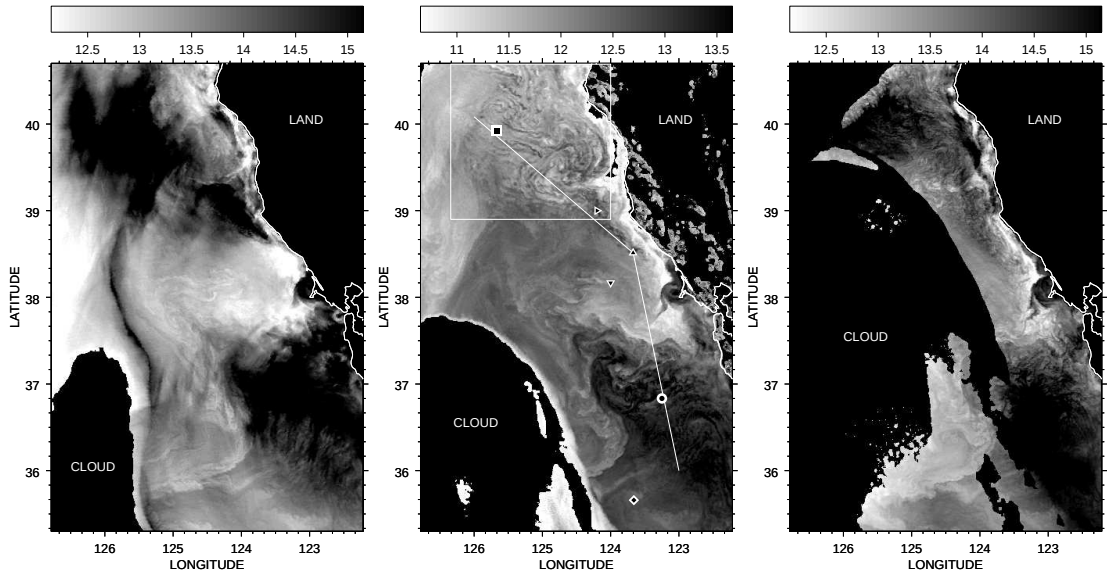

Figure 8: Thermal infrared images: (a) 21 April 1982 22:53 UT (NOAA-7), (b) 22 April 1982 11:17 UT (NOAA-7), (c) 22 April 1982 22:41 UT (NOAA-7). Land and clouds are masked. Light gray shades correspond to cold water. The positions of the section shown in Fig. 9, of the samples shown in Fig. 11, and of the area enlarged in Fig. 12 are overlaid on (b).

3 Satellite measurements

Four 1-km resolution Advance Very High Resolution Radiometer (AVHRR) images were acquired at the Scripps Satellite Oceanography Facility, on 21 April at 22:53 UT (NOAA-7), and on 22 April at 11:17 (NOAA-7), 16:43 (NOAA-6) and 22:41 UT (NOAA-7) respectively, spanning a full diurnal cycle. The times of the images are indicated as dotted lines on Figs. 3 and 7. Note that the afternoon images were taken at ∼14:30 LST, approximately the mean time of the peak of the diurnal cycle [Price *et al.*, 1987, their Fig. 8].

The final calibrated cloud-masked thermal infrared images are shown in Fig. 8; the corrections applied are discussed in the Appendix. A bank of stratus clouds originated from the southwest, progressively filling the images, but there were no scattered convective clouds. Fig. 9 shows temperature variations along a section through the images. For the afternoon images, the visible channel albedo along these sections was nearly constant at 2%, confirming that the corresponding pixels were cloud-free.

In the afternoon of 20 April (Fig. 8a), two intense warm pools had formed, one to the west of Cape Mendocino, centered on 125°30W 40°N, the other one to the west of Santa Cruz, centered on 123°30W 37°N, each with a diameter of ∼100 km and surface temperature peaking at 18 C. Between the warm pools, a zonal band of colder water at ∼12.5 C extended meridionally from 37°30N to 38°30N. A smaller and less intense warm pool had also formed closer to the coast near Point Arena (124°N 39°W), reaching the edge of the CODE domain. Worth noting is a narrow meridional ribbon of warm water, extending along 125°30W from 35°30N to 39°00N, at most 10-

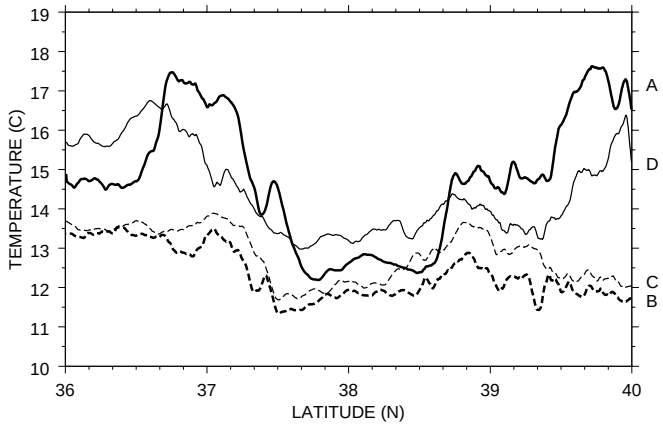

Figure 9: Temperature along the section shown in Fig. 8b. **A** is 21 April 1982 22:53 UT, **B** is 22 April 1982 11:17 UT, **C** is 22 April 1982 16:43 UT and **D** is 22 April 1982 22:41 UT. The two warm pools are centered near 37°N and 40°N.

km wide.

By the middle of the following night (Fig. 8b), the warm pools and the warm ribbon had mostly disappeared: the temperature variations were closer to the climatological north to south gradient, with some distortions due to mesoscale eddies. The temperature field was similar the next morning (not shown). In the afternoon of 21 April (Fig. 8c), the two warm pools had formed again, reaching 17 C, but their exact shapes and positions had changed.

Two-dimensional histograms of pairs of images are shown in Fig. 10. The correlation is excellent between the night and the morning images (Fig. 10b). Between the night image and the afternoon images (Fig. 10a and 10c), the two warm pools appear as two distinct off-diagonal lobes, the northern one centered at 12 C on the night image axis, reaching 18.3 C the first afternoon and 17.6 C the second, and the southern one centered at 13.3 C, reaching 17.8 C and 17.2 C. The poor correlation between the two afternoon images (Fig. 10d) illustrates the rapidly changing shapes and positions of the warm pools.

Time series of surface temperature from the images (Fig. 11) were obtained by computing the median temperature in $30 \times 30\mathrm{km}^2$ squares centered at each sampling point. Outside or at the edge of the warm pools, the diurnal variation is less than 1.3 C. In the warm pools, the diurnal cycle reaches 5.5 C amplitude, which may be underestimated by the median: some isolated patches have in fact an astounding amplitude of 6.6 C!

Enlarged images of the northern warm pool are shown in Fig. 12. A closer inspection of the night image (Fig. 12b) reveals intricate temperature patterns where the warm pools had formed the previous afternoon. Temperature varies rapidly over short scales, displaying numerous streaks, typically $\sim$50 km long, with a characteristic wavelength of 4 to 8 km. The boundaries of the area where the streaks are seen correspond roughly to the previous boundaries of the warm pool. The streaks are still present in the following morning and afternoon images (Figs. 12c and d), albeit attenuated, but the same patterns persist where the amplitude is the strongest (for example, in the vicinity of 125°W 39°15N).

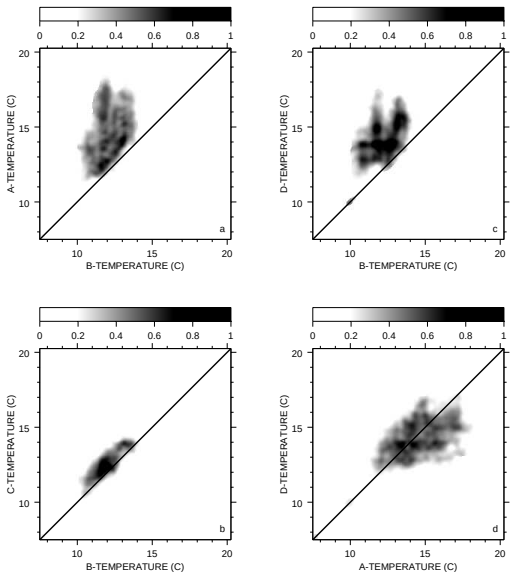

Figure 10: Two-dimensional histograms of AVHRR temperatures. **A**, **B**, **C** and **D** are defined in Fig. 9. (a) **A** vs. **B**, (b) **C** vs. **B**, (c) **D** vs. **B**, (d) **D** versus **A**. The gray scale represents the log frequency normalized to the largest value.

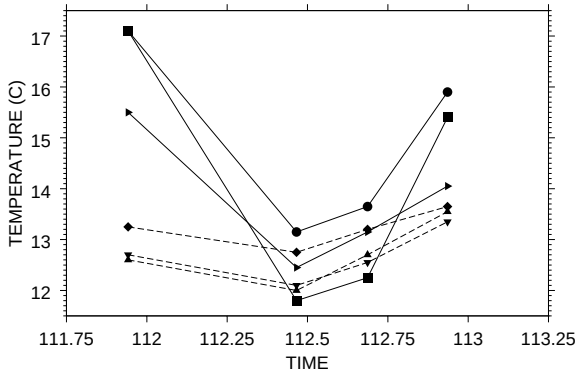

Figure 11: Time series of the median temperatures over $1000\mathrm{km}^2$ squares centered on the sampling points shown in Fig. 8b. Solid: warm pools. Dashed: "windy" areas.

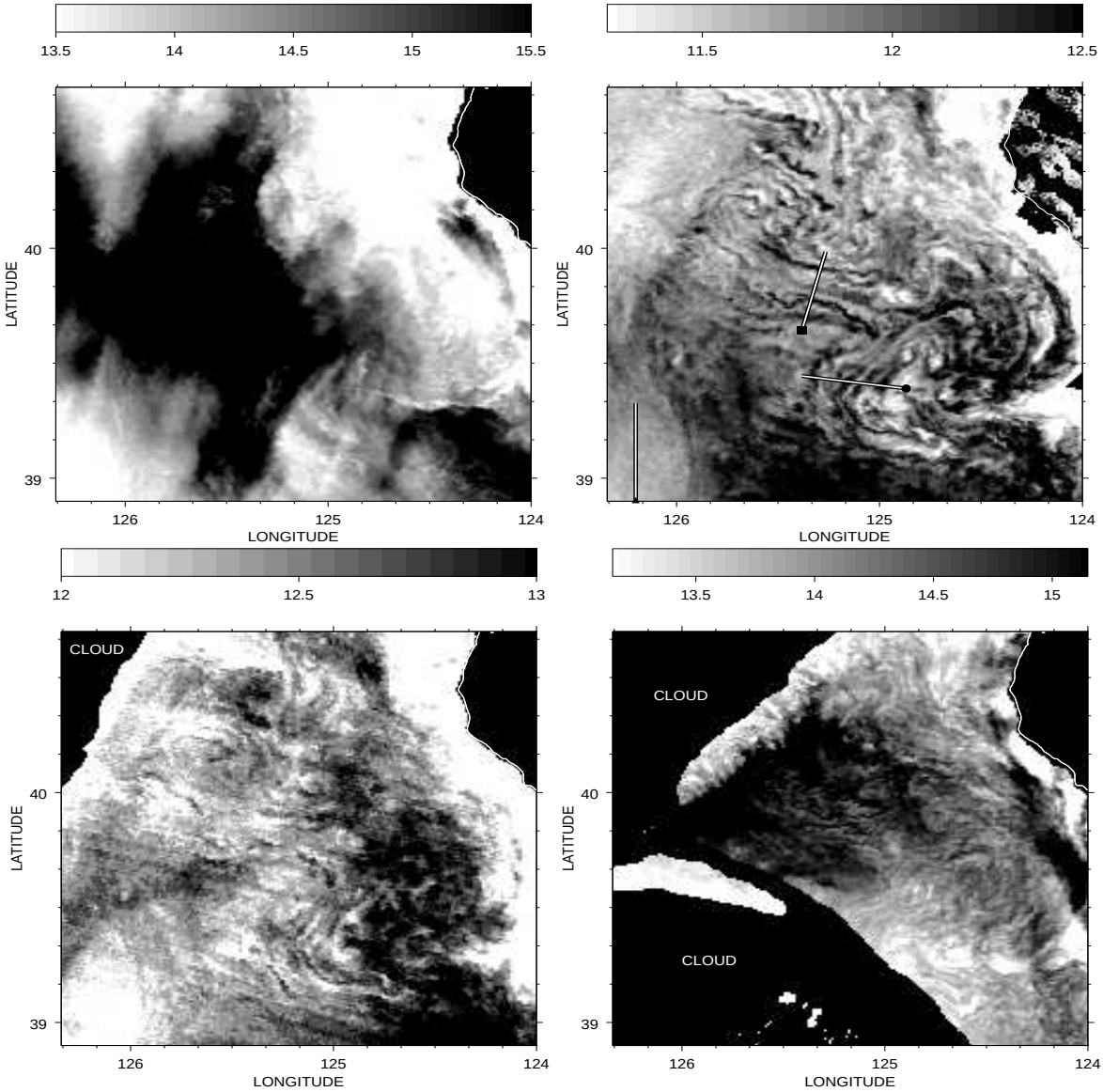

Figure 12: Enlarged images of the northern warm pool: (a) 21 April 1982 22:53 UT, (b) 22 April 1982 11:17 UT, (c) 22 April 1982 16:43 UT and (d) 22 April 1982 22:41 UT. Notice the striking difference of temperature structure between (a) and (b). The positions of the sections shown in Fig. 13 is overlaid on (b).

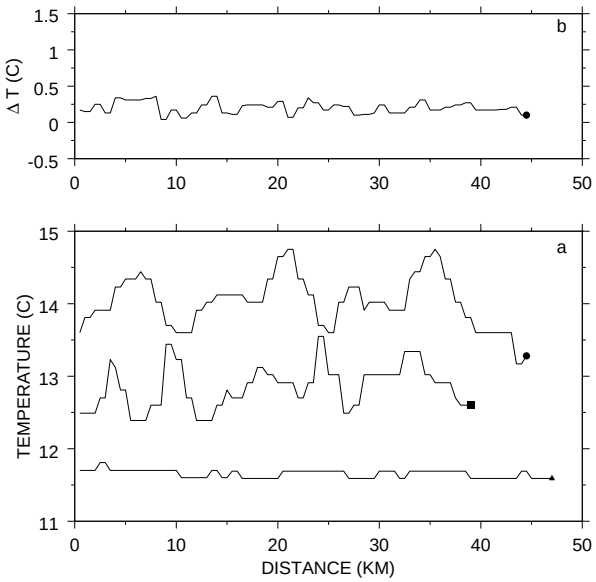

Figure 13: (a) temperature at 11:17 UT on 22 April 1985 along the sections overlaid on Fig. 12b, starting clockwise from the southernmost section (successive plots are shifted 1 C up); notice the periodic variations of $\sim$1 C peak-to-peak. (b) difference between the 10.8μm and 12.0μm channels for the third section.

Sections across the night image (Fig. 12b) are shown in Fig. 13a, to contrast the $\sim$1.0 C peak-to-peak temperature variations crossing the streaks, with those less than 0.2 C in the homogeneous area to the west. The difference between the thermal infrared channels at 10.8μm and at 12.0μm is also shown in Fig. 13b. It is sensitive to atmospheric water vapor, which absorbs more at 12.0μm than at 10.8μm. This difference does not display variations correlated with the streaks, indicating that the streaks were not an artifact caused by variable humidity.

At night, clouds can be detected by their emissivity, lower at 3.7μm ($\sim$0.70) than at 10.8μm or 12.0μm (0.99) [Hunt, 1973]. For example, the cloud bank to the southwest of Fig. 8b has a mean radiometric temperature of 10.5 C in the 10.8μm channel, but of only 3.5 C in the 3.7μm channel. Unfortunately, this channel is contaminated by interference noise from the NOAA-7 spacecraft, with a peak-to-peak amplitude of 1.5 C and an along-scan wavelength of about 15 pixels (or km), completely obliterating the streaks. The average temperature along the third section is 10.3 C in the 3.7μm channel and 10.7 C in the 12.0μm channel. This indicates that the streaks are not clouds, because clouds thick enough to be colder than the ocean in the 12.0μm channel, would have a 3.7μm channel temperature offset much larger than the instrument noise.

Nimbus-7 Coastal Zone Color Scanner (CZCS) images from the West Coast Time Series [Abbott and Zion, 1987] are available for 21 April 1982 at 20:11 UT and 23 April 1982 at 19:04 UT. Fig. 14 shows the image of the 490-nm diffuse attenuation coefficient κ_a on 21 April, about 2.5 hours before the first AVHRR image. The corresponding section for optical depth is shown in Fig. 15 (*cf.* Fig. 9b). The CZCS image for 23 April (not shown) is mostly cloudy, except towards the southeast, where it is virtually identical to the image on 21 April, within small advective changes.

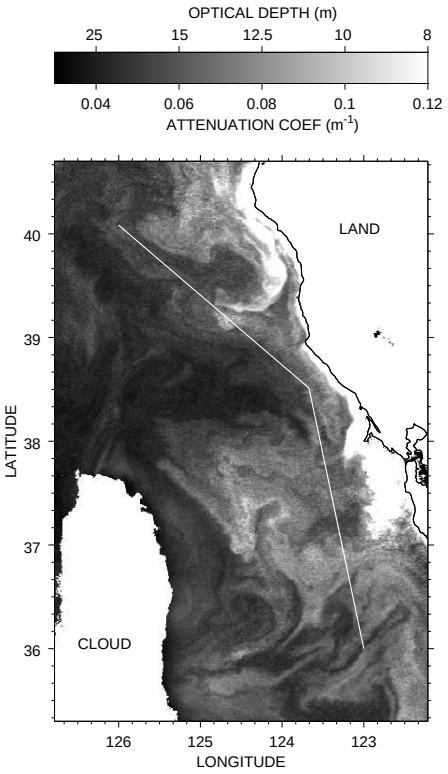

Figure 14: Image of the 490-nm diffuse attenuation coefficient from the CZCS on 21 April 1982 20:11 UT. Light gray shades correspond to clear water (small coefficients); the calibration wedge is in m^{-1}. The position of the section shown in Fig. 15 is overlaid.

. The two offshore warm pools correspond to κ_a^{-1} varying between 15 m and 25 m. Similar values are observed in the zonal band of cold water, identified between 37°30N and 38°30N in Fig. 8a. These values correspond to a fairly clear water (Jerlov type Ia or II). The peaks of higher pigment observed at 37°N and 39°10N correspond to small upwelling filaments advecting high-productivity coastal water offshore, unrelated to the diurnal warming process studied here.

The two-dimensional histogram of the temperature difference between the first afternoon image and the night image, versus the diffuse attenuation coefficient from the CZCS image, is shown in Fig. 16. There is no correlation between the two fields, suggesting that the warm pools did not correspond to areas of unusually large phytoplankton concentration.

4 Summary

Satellite and *in situ* data were used to document an intense case of diurnal warming off California in Spring 1982. We found that:

1. warming patches formed in an area of low wind, apparently responding to details of the wind field not seen in the synoptic pressure map;

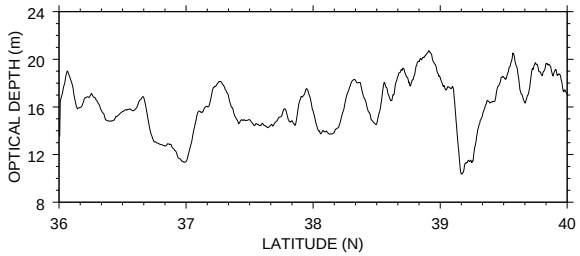

Figure 15: Optical depth and pigment concentration from the CZCS along the section shown in Fig. 14 (see, also, Fig. 9).

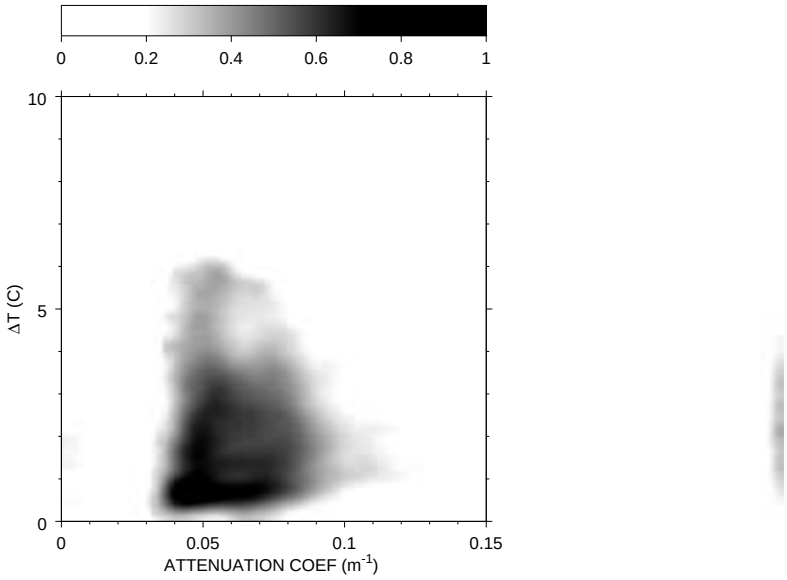

Figure 16: Two-dimensional histogram of the AVHRR diurnal temperature amplitude (difference between images **A** and **B** as defined in Fig. 9), versus the diffuse attenuation coefficient from the CZCS image shown in Fig. 14. The gray scale represents the log frequency normalized to the largest value.

2. during the period of no wind mixing, the heat that entered the ocean remained trapped within the upper 25 m;

3. the amplitude of the diurnal cycle of surface temperature reached 6.6 C in the warming patches, corresponding to a shallow trapping depth of 0.68 m;

4. the warming patches did not correspond to an area of unusually shallow optical depth, suggesting that pigment concentration did not govern the heat trapping;

5. coherent horizontal surface temperature streaks formed during the subsequent nocturnal erosion of the warming patches, with wavelengths of 4 to 8 km and peak-to-peak amplitudes of 0.5 to 1.5 C.

5 Discussion

5.1 Horizontal extent

The spatial extent of diurnal warming has been documented in the North Atlantic by Cornillon and Stramma [1985], and Stramma *et al.* [1986], who compared NOAA-7 images with synoptic weather maps. The warming patches always corresponded to anticyclonic ridges, but modulations of the warming amplitude at scales not resolved by the synoptic pressure field were present. Similarly, Deschamp and Frouin [1984] confirmed the relationship between atmospheric anticyclones and diurnal warming events in the Western Mediterranean Sea. Our observations are consistent with their results, and show that the shapes and positions of warming patches varies rapidly in response to the evolution of the wind field.

5.2 Trapping depth and amplitude

The diurnal amplitude of the warm pools was astounding, reaching 6.6 C in the satellite images, and 5.05 C (possibly underestimated) in the mooring time series. Based on the net daily heat input of $18 \mathrm{MJ m^{-2}}$, (*cf.* Fig. 6), this amplitude translates into a trapping depth of $\sim$68 cm! Extreme amplitudes exceeding 4 C were also reported by Stramma *et al.* [1986] for the Sargasso sea and by Ramp *et al.* [1991] off California.

As pointed out by Cornillon and Stramma [1985], air-sea heat fluxes estimated using ship engine intake temperature (at $\sim$3-5 m depth) or even moored surface buoy temperature (at $\sim$0.5-1 m depth) will be biased when extreme surface heat trapping occurs. The outgoing thermal infrared radiation, and the sensible and latent heat fluxes based on bulk parametrizations, are all function of water temperature, and will all underestimate the cooling of the surface, unless the water temperature is measured within the trapping layer. For the conditions discussed in section 3, the total bias would be $\sim 55 \mathrm{W m^{-2}}$ for a 1 m/s wind, of which $30 \mathrm{~W m^{-2}}$ would be due to the outgoing radiation.

The diurnal cycle of temperature can obey two different regimes: in the wind regime, vertical mixing results from instability of the wind-driven shear, whereas in the so-called radiative-convective regime, mixing is driven by convective instability of the surface layer, cooled at the surface but heated at depth by solar radiation. The diurnal amplitudes observed were generally larger than given by the empirical least square fit given by Price *et al.* [1987] for the wind regime, suggesting that the warm pools were principally obeying the radiative-convective regime.

In the later case, the trapping depth and the diurnal amplitude can be computed exactly if the irradiance profile is known [Dalu and Purini, 1982]. Assuming the bi-exponential profile used at the end section 2, the balance between the cooling flux L_0 applied at the surface and the heating flux absorbed at depth yields a convective mixed-layer of thickness z_c given by the solution of

$$R(\zeta_1 z_c - 1)\exp(\zeta_1 z_c) + (1 - R)(\zeta_2 z_c - 1)\exp(\zeta_2 z_c) = \frac{L_0}{I_0} - 1. \quad (1)$$

For $I_0 = 850\mathrm{W m^{-2}}$, $L_0 = 70\mathrm{W m^{-2}}$, and a Jerlov type II water with $\zeta_1^{-1} = 1.5\mathrm{m}$, $\zeta_2^{-1} = 14\mathrm{m}$ (consistent with Fig. 14), and $R = 0.77$, one obtains $z_c = 0.83\mathrm{m}$, in fair agreement with the estimated trapping depth given the lack of *in situ* measurement of the irradiance profile.

The concentration of phytoplankton may affect the absorption of heat in the upper ocean, potentially yielding anomalies of the temperature profiles [Lewis *et al.*, 1983; Dickey and Simpson, 1983; Morel, 1988]. Ramp *et al.* [1991] recently proposed that strong temperature gradients reaching 4.7 C over the upper 2 m, observed in coastal waters off California under near-zero wind stress, were caused by high water turbidity, and that horizontal temperature variations in these warming layers may have been caused by patchiness of the chlorophyll concentration. The fairly clear waters inferred from the CZCS images where the warm pools formed (κ_a^{-1} ~18 m for the northern warm pool and ~14 m for the southern warm pool) indicate that, at least for the particular event described here, a large pigment concentration was not necessary to obtain the shallow heat trapping.

5.3 Coherent streaks

A new finding is the formation of coherent streaks, apparently associated with the erosion and decay of warming layers during the night following a strong event. These streaks are quite common under low wind conditions off California; in addition to the event reported here, they were subsequently observed in July 1985 by Flament [1989], in June 1987 by Ramp *et al.* [1991] and in July 1988 by Abbott [personal communication]. They can (barely) be seen in Fig. 12 of Strub *et al.* [1991].

Deschamps *et al.* [1984] first pointed out the occurrence of filamentous surface temperature patterns in the Mediterranean sea under low wind conditions (their Fig. 13b). These patterns were presumably similar to the streaks observed off California. Unfortunately, they lacked *in situ* data to interpret their observations in terms of diurnal warming layers.

Do similar streaks form during diurnal warming events in the Sargasso Sea? Cornillon and Stramma [1985] do not describe any, but the heavy filtering scheme used in their processing (4x4 subsampling followed by 5x5 median) may have obliterated the signature of the streaks, if they existed. AVHRR images of diurnal warming events in the Sargasso Sea should be reexamined at full 1-km resolution, to establish whether or not coherent temperature streaks occur there as well.

What known upper ocean processes might be responsible for these variations of surface temperature? Possible candidates are internal waves and convective motions in the oceanic mixed layer.

Internal waves are often present at the interface between the mixed layer and the seasonal thermocline. Similar interfacial waves are often observed near shore under highly stratified conditions [LaFond, 1962]. The divergent crests of these waves would bring colder water near the surface, revealing them to the satellite radiometer. For $\Delta\rho = 1\mathrm{kg m^{-3}}$ and $h = 65\mathrm{m}$ (*cf.* Fig. 4), the phase speed of these waves would be $(gh\Delta\rho/\rho)^{\frac{1}{2}} \sim 0.8\mathrm{ms^{-1}}$, propagating ~15 km between the night

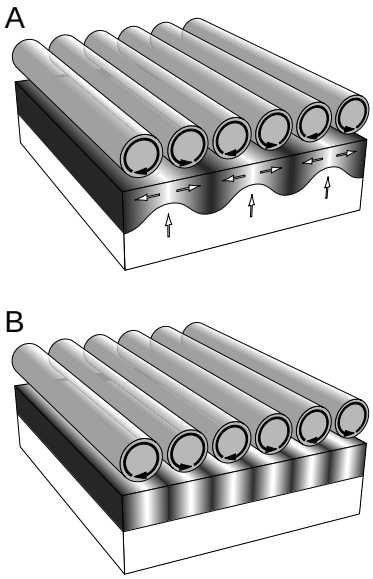

Figure 17: Conceptual sketch of the proposed scenarios for the formation of temperature streaks. (a) ocean response in the mixing-driven scenario, (b) ocean response in the advection-driven scenario.

and morning images. The patterns seen in Figs. 12b and 12c near 125°W 39°15N, stationary within a few kilometers, do not appear consistent with propagating interfacial waves.

Convection within the mixed layer would also bring colder water near the surface. Langmuir cells [Weller and Price, 1988] can be excluded, because they form in wind and wave conditions too energetic to allow the formation of diurnal warming layers. Buoyant convection might occur during nocturnal cooling, but would create surface temperature patterns at a horizontal wavelength a few times the mixed layer thickness, or 50-200 m, in contradiction with the 4 to 8 km scale observed.

The scale of the streaks does not appear consistent with processes involving the upper ocean alone, and instead points to a coupling with the atmospheric boundary layer. Helical circulation rolls occur frequently in the boundary layer, deriving their energy from a combination of convective forcing and instability of the vertical shear [Brown, 1980]. Their wavelength is typically 2 to 4 times the ~1 km boundary layer thickness. These circulation rolls modulate the surface wind stress, with maxima along the axes of the rolls, and minima along the stagnation lines beneath downdrafts and updrafts. Two scenarios for the formation of temperature streaks in the ocean can therefore be hypothesized.

If surface temperature is principally governed by one-dimensional wind-driven mixing of warm layers with deeper water, cold anomalies would form beneath the axes of the rolls where the wind stress is strongest, and temperature streaks at one-half the wavelength of the rolls would appear (Fig. 17a).

If surface temperature is principally governed by wind-driven horizontal advection, warming layers would thicken beneath convergent updrafts, and become thinner or even disappear beneath divergent downdrafts, resulting in cold temperature streaks at the wavelength of the rolls (Fig. 17b). A feedback mechanism is then possible, in which the air would be heated by the surface beneath the

updrafts and cooled beneath the downdrafts, fueling the convective rolls and spatially locking them to the temperature streaks. This mechanism would act to limit the diurnal amplitude, enhancing the surface latent and sensible heat fluxes through increased atmospheric convection.

In both scenarios, the scale of the surface temperature variations would be imposed by the atmospheric rolls. These scenarios, of course, are speculative, and must await detailed observations of the sub-mesoscale wind field and of the atmospheric stratification under very low wind conditions to be refuted or confirmed.

Acknowledgements

C. Alessi gave us the CODE data and R. Ossinger the CZCS data. R. Bernstein provided a pre-release version of the $Terascan$ image processing software and D. Kelley made available his outstanding plotting package *gri*, which was used for all the figures. Brooks Bays and Nancy Hulbirt designed Fig. 17. Our work has benefited from discussions with Mark Abbott, Larry Armi, Peter Cornillon, Steve Lentz, Jim Price and Bob Whritner. This manuscript owes its existence to the scepticism of Russ Davis ("*these streaks are just clouds*") and to the enthusiasm of Myrl Hendershott ("*you must absolutely document this*"). Analysis supported by the Office of Naval Research through contract N000014-87-K-007 to WHOI, and by the National Science Foundation through grants OCE-8918604 and REU-8900858 to UH.

References

Abbott, M. and Zion, P., (1987). Spatial and temporal variability of phytoplankton pigment off northern California during CODE. *J. Geophys. Res.*, **92**, 1745–1755.

Beardsley, R., Dorman, C., Friehe, C., Rosenfeld, L., and Winant, C., (1987). Local atmospheric forcing during CODE: a description of the marine boundary layer and atmospheric conditions over the Northern California upwelling region. *J. Geophys. Res.*, **92**, 1,467–1,488.

Brown, R., (1980). Longitudinal instabilities and secondary flows in the planetary boundary layer: a review. *Rev. Geophys. and Space Phys.*, **18**, 683–697.

Bruce, J. and Firing, E., (1974). Temperature measurements in the upper 10 m with modified expandable bathythermograph probes. *J. Geophys. Res.*, **79**, 4,110–4,111.

Cornillon, P. and Stramma, L., (1985). The distribution of diurnal warming events in the western Sargasso Sea. *J. Geophys. Res.*, **90**, 11,811–11,815.

Dalu, G. and Purini, R., (1982). The diurnal thermocline due to buoyant convection. *Quart. J. Roy. Meteor. Soc.*, **108**, 929–935.

Deschamps, P., Frouin, R., and Cŕepon, M., (1984). Sea surface temperatures of the coastal zones of France observed by the HCMM satellite. *J. Geophys. Res.*, **89**, 8123–8149.

Dickey, T. and Simpson, J., (1983). The influence of optical water type on the diurnal response of the upper ocean. *Tellus*, **35B**, 142–154.

Flament, P., (1989). Observations of the horizontal structure of the surface layer of the ocean under low wind conditions. In *Proceedings of the IGARSS'89 Conference*, pages 318–322. I.E.E.E., New York.

Fleischbein, J., Gilbert, W., and Huyer, A., (1983). Hydrographic data from CODE-2: R/V We-

coma, leg 6, 18-24 april 1982. Technical Report 83-4, Oregon State University, School of Oceanography.

Hunt, G. E., (1973). Radiative properties of terrestrial clouds at visible and infra-red thermal window wavelengths. *Quart. J. Roy. Meteor. Soc.*, **99**, 346–369.

LaFond, E., (1962). Internal waves (part I). In Hill, M., editor, *The Sea*, volume 1. Intersci, New York.

Lentz, S., (1987). A heat budget for the northern California shelf during CODE-2. *J. Geophys. Res.*, **92**, 14,491–14,509.

Lewis, M., Cullen, J., and Platt, T., (1983). Phytoplankton and thermal structure in the upper ocean: consequences of nonuniformity in chlorophyll profile. *J. Geophys. Res.*, **88**, 2565–2570.

Limeburner, R., (1985). CODE-2: moored array and large-scale data report. Technical Report WHOI 85-35, Woods Hole Oceanographic Institution, Woods Hole, Mass.

Morel, A., (1988). Optical modeling of the upper Ocean in relation to its biogenous matter content (case i waters). *J. Geophys. Res.*, **93**, 10749–10768.

Price, J., Weller, R., and Pinkel, R., (1986). Diurnal cycling: observations and models of the upper ocean response to diurnal heating, cooling and wind mixing. *J. Geophys. Res.*, **91**, 8411–8427.

Price, J., Weller, R., Bowers, C., and Briscoe, M., (1987). Diurnal response of sea surface temperature observed at the LOTUS in the sargasso sea. *J. Geophys. Res.*, **92**, 14480–14490.

Ramp, S., Garwood, R., Davis, C., and Snow, R., (1991). Surface heating and patchiness in the coastal Ocean off central California during a wind relaxation event. *J. Geophys. Res.*, **96**, 14947–14957.

Stramma, L., Cornillon, P., Weller, R., Price, J., and Briscoe, M., (1986). Large diurnal sea surface temperature variability: satellite and in-situ measurements. *J. Phys. Oceanogr.*, **16**, 827–837.

Strub, P., Kosro, P., and Huyer, A., (1991). The nature of cold filaments in the California current system. *J. Geophys. Res.*, **96**, 14,743–14,768.

Weller, R. and Price, J., (1988). Langmuir circulation within the oceanic mixed layer. *Deep-Sea Res.*, **35**, 711–747.